



# WFIRST and EUCLID: Enabling the Microlensing Parallax Measurement from Space

Etienne Bachelet<sup>1</sup> and Matthew Penny<sup>2</sup> <sup>1</sup> Las Cumbres Observatory, 6740 Cortona Drive, Suite 102, 93117 Goleta, CA, USA; [etibachelet@gmail.com](mailto:etibachelet@gmail.com)<sup>2</sup> Department of Astronomy, The Ohio State University, 140 West 18th Avenue, Columbus, OH 43210, USA

Received 2019 May 28; revised 2019 June 24; accepted 2019 June 26; published 2019 August 1

## Abstract

The *Wide Field Infrared Survey Telescope* (WFIRST) is expected to detect hundreds of free-floating planets, but it will not be able to measure their masses. However, simultaneous microlensing observations by both *Euclid* and WFIRST, separated by  $\sim 100,000$  km in orbits around the Sun–Earth L2 Lagrange point, will enable measurements of microlensing parallax for low-mass lenses such as free-floating planets. Using simple Fisher matrix estimates of the parallax measurement uncertainties, we show that high-cadence observations by *Euclid* could be used to measure  $\sim 1$  free-floating planet microlens parallax per 6 days of simultaneous *Euclid* observations. Accounting for *Euclid*'s pointing constraints, it could therefore potentially measure  $\sim 20$  free-floating planet parallaxes, with 120 days of observations split equally between *Euclid*'s main mission and an extended mission, with the potential to increase this number if spacecraft pointing constraints can be relaxed after the end of the main mission. These *Euclid* observations would also provide additional mass measurements or cross-checks for larger numbers of WFIRST's bound planets, among other benefits to several science cases.

*Key words:* gravitational lensing: micro – parallaxes

## 1. Introduction

Gravitational microlensing is a formidable tool for exploring the population of non-luminous objects. Originally applied to the detection of Massive Compact Halo Object (MACHO) dark matter (Paczynski 1986; Alcock et al. 1993; Aubourg et al. 1993; Udalski et al. 1993), microlensing surveys have significantly increased their sky coverage and observing cadence in the past decade in order to search for exoplanets (Gaudi 2012). This has led to the discovery of a wide variety of bound exoplanets (e.g., Bond et al. 2004; Beaulieu et al. 2006), brown dwarfs (see, e.g., Bachelet et al. 2019, and references therein), binary stars (e.g., Han et al. 2018), and stellar remnant candidates (e.g., Shvartzvald et al. 2015; Wyrzykowski et al. 2016).

Microlensing is especially powerful at detecting isolated planetary mass objects, so-called free-floating planets (Oasa et al. 1999; Zapatero Osorio et al. 2000; Luhman et al. 2005; Burgess et al. 2009; Marsh et al. 2010). Sumi et al. (2011) claimed the discovery of a large population of unbound or large separation (i.e.,  $\geq 100$  au) planets from measurements of the microlensing timescale distribution. This population of Jupiter-mass objects would have to be twice as common as main-sequence stars, which is an occurrence rate of about an order of magnitude larger than predicted by planet formation models (Veras & Raymond 2012; Ma et al. 2016). However, more recent timescale distribution measurements (Mróz et al. 2017; OGLE Collaboration et al. 2019) refute a large population of massive planets but indicates a potential population of less massive free-floating planets that would be observable with space-based microlensing surveys (e.g., Barclay et al. 2017).

In many cases a clear interpretation of a microlensing event has relied on mass–distance relations from the detection of microlensing parallax  $\pi_E$ , and measurement of the angular Einstein ring radius  $\theta_E$ . Together these observables allow the measurement of the distance of the lens  $D_l$  and the mass of the

lens (e.g., Gould 2000)

$$M_l = \frac{\theta_E}{\kappa \pi_E}, \quad (1)$$

where  $\kappa = 8.144 \text{ mas } M_\odot^{-1}$ . Without constraints on the microlens parallax or angular Einstein radius, the only information about the mass of the lens is provided by the Einstein radius crossing time, or more succinctly the event timescale

$$t_E = \frac{\theta_E}{\mu_{\text{rel}}}, \quad (2)$$

from the light curve of the microlensing event, where  $\mu_{\text{rel}}$  is the relative lens–source proper motion. The angular Einstein radius,

$$\theta_E = \sqrt{\kappa M \frac{1 - D_l/D_s}{D_l}}, \quad (3)$$

depends on the mass as well as the lens and source distances,  $D_l$  and  $D_s$ , respectively, so the timescale is a degenerate combination of the lens mass, distances, and relative proper motion of the lens and source.

Often,  $\theta_E$  is derived from finite source effects visible in the light curve (Witt & Mao 1994), but can also be measured with high-resolution imaging (e.g., Bennett et al. 2007). Microlensing parallax can be measured by the subtle effect of an accelerating observer on the light curve (so-called annual parallax), but generally requires timescales of  $\gtrsim 50$  days for the effects to be detectable (e.g., Poindexter et al. 2005). Alternatively, observations of a microlensing event from two well separated locations ( $\sim \text{au}$ ), the so-called satellite parallax, can yield a measurement of microlensing parallax (e.g., Refsdal 1966; Gould 1994; Henderson et al. 2016; Zhu et al. 2017). Measurement of the microlensing parallax alone is also a precious tool for exploring the mass distribution toward the Galactic Bulge (Calchi Novati et al. 2015). Note that accurate photometry is of first importance to obtain strong constraints on

the microlensing parallax from space, as recently pointed by Koshimoto & Bennett (2019).

Two of the primary goals of the *Wide Field Infrared Survey Telescope* (*WFIRST*) space mission are to study dark energy via wide-field imaging and spectroscopic surveys (Spergel et al. 2015), and to conduct a large statistical survey of exoplanet demographics using microlensing (Penny et al. 2019). The masses of most *WFIRST* bound planets and their hosts will be estimated via measuring the amplitude and direction of the relative proper motion and the measurement of the lens flux with high-resolution imaging (e.g., Bhattacharya et al. 2018). However, some planet hosts will be too faint, or will not move far enough away from bright source stars, to be detected. In these cases, microlens parallax can provide a mass measurement, and even if lens light is detected a parallax measurement can provide a vital cross check on the lens-light-derived mass, which can be contaminated by light from other stars.

For free-floating planets, *WFIRST* alone will not be able to measure their masses because they will emit essentially no light, and their  $\lesssim 1$  day event timescales are too short to measure annual parallaxes as presented in the following. However, in many of its free-floating planet events *WFIRST* will detect finite source effects and measure  $\theta_E$  (S. Johnson et al. 2019, in preparation). Therefore, if their microlens parallax can be measured via satellite parallax, it is possible to measure the free-floating planets' masses. Unfortunately, the short timescale of free-floating planet events makes it impossible to coordinate follow-up observations in time to catch the event, so only wide-field high-cadence observations can be used for this task. While simultaneous ground-based observations with *WFIRST* have been suggested (e.g., Zhu & Gould 2016; Street et al. 2018), they face extraordinary challenges to be able to effectively observe the extremely faint microlensing events that *WFIRST* will find (see Figure 3), even for the Large Synoptic Survey Telescope (Abell et al. 2009), if *WFIRST* fields are selected at in high-extinction regions.

*Euclid*, the European Space Agency mission with the singular goal of characterizing dark energy via wide-field surveys of the extragalactic sky (Laureijs et al. 2011), has wide-field imaging capabilities that are similar to those of *WFIRST*. Penny et al. (2013) showed that *Euclid* will be well suited to conducting exoplanet microlensing searches, and significantly more capable than ground-based searches. In this Letter, we show how a modest investment of *Euclid*'s time to obtain observations simultaneously with *WFIRST*'s microlensing survey observations is the only way to measure the parallaxes of microlensing events due to telluric free-floating planets predicted by star formation theories.

## 2. Fisher Matrix Parallax Uncertainties and Observational Parameters

To study the potential of simultaneous *Euclid* and *WFIRST* microlensing observations, we used the Fisher matrix formalism (Gould 2013; Mogavero & Beaulieu 2016; Bachelet et al. 2018) to estimate the precision of parallax measurements of microlensing events observed by both spacecraft. Based on this formalism, Mogavero & Beaulieu (2016) defines the minimum

error parallax measurement  $\sigma_{\pi_E, \min}$  as

$$\sigma_{\pi_E, \min}^2(\phi) = \frac{\sigma_{\pi_{\parallel}}^2 + \sigma_{\pi_{\perp}}^2}{2} - \frac{\sqrt{(\sigma_{\pi_{\parallel}}^2 - \sigma_{\pi_{\perp}}^2)^2 + 4 \text{cov}(\pi_{\parallel}, \pi_{\perp})^2}}{2}, \quad (4)$$

with  $\sigma_{\pi_{\parallel}}$ ,  $\sigma_{\pi_{\perp}}$ , and  $\text{cov}(\pi_{\parallel}, \pi_{\perp})$  as the error on the parallel and perpendicular components of the parallax vector and their mutual covariance. To compute the Fisher covariance matrix we assume that the microlensing events are single-lens events with no finite source effects.<sup>3</sup> Following Mogavero & Beaulieu (2016), we assume that the photometric noise level  $\sigma$  at the baseline is a free parameter. We also assume that there is no blending from isolated stars (but, as described below, we do include a smooth background due to unresolved stars when estimating photometric precision).

We assume *WFIRST* observations are taken continuously within an observing window of 70 days. We consider microlensing events with a peak time  $t_0$  set to be the center of the *WFIRST* observations. *Euclid* will have more restrictive observing constraints and can only observe the same fields as *WFIRST* continuously for 20 days in a window centered 10 days earlier or later than *WFIRST*'s window center (Gómez-Alvarez et al. 2018).

Both telescopes are assumed to be orbiting the L2-point with a circular orbit of radius  $R = 300,000$  km, an orbital period  $P$  of 180 days, and separated by a phase  $\phi$ . These parameters are broadly representative of spacecraft orbits around L2, and we will consider the impact of changing the spacecraft separation in Section 4. We consider the microlensing source to be in the Galactic Bulge (i.e.,  $D_s = 8$  kpc) and a relative source-lens transverse velocity  $V = 200 \text{ km s}^{-1}$ . The angle  $\theta$  between the source trajectory and the projected East vector on the plane of sky is set to 45deg (see Bachelet et al. 2018 for more details on the geometry of the problem). The latitude of the microlensing event relative to the orbital plane of the spacecraft about L2 is set to 30 deg. Finally, the lens is assumed to be at 4 kpc, leading to a direct relation between the event timescale, the microlens parallax,

$$\pi_E = 4.3 \left( \frac{1\text{D}}{t_E} \right), \quad (5)$$

and the lens mass

$$M = 0.87 M_{\text{Jup}} \left( \frac{t_E}{1\text{D}} \right)^2. \quad (6)$$

Note that the lens distance has a significant impact on the magnitude of the parallax; our choice of a single value is designed to simplify the parameter space while providing a reasonable quantitative estimate of parallax detectability.

Bachelet et al. (2018) considered the L2-point to be inertial and ignored the effect of the annual parallax. To challenge this assumption we use Equation (16) of Gould (2013) to estimate the uncertainty of a one-dimensional annual parallax measurement for a short, reasonably high-magnification microlensing

<sup>3</sup> The assumption of no finite source effects does not always apply, but every case where it does not (either high magnification or low planet masses) is generally favorable to measuring parallax.

event. We can combine this with our rough scaling for  $\pi_E$ , and the cadence of *WFIRST* observations, to estimate the minimum event timescale for which annual parallax can provide interesting constraints. Bachelet et al. (2018) also shown that the Fisher matrix formalism can be optimistic, therefore we require a  $5\sigma$  constraint on the  $1-d$  parallax, i.e.,  $5\sigma_{\pi_E, 1-d} < \pi_E$ . The annual parallax constraints are only possible if

$$t_E \gtrsim 3.6 \text{ days} \left( \frac{\sigma}{0.01 \text{ mag}} \right)^{2/3}, \quad (7)$$

where  $\sigma$  is the photometric precision of *WFIRST* at the baseline. Therefore, the acceleration of the Lagrangian point L2 around the Sun is insufficient to constrain the parallax for low-mass lenses, especially for free-floating planets. To confirm this, we apply the Fisher formalism to the motion of *WFIRST* around the Sun. The detection limits of microlensing parallax measurements by *WFIRST* alone due to annual parallax are shown in red in Figures 2 and 3. These calculations confirm that *WFIRST* alone will not measure the parallax for events with  $t_E \leq 4$  days.

### 3. *WFIRST* and *EUCLID* Noise Model

We assume that *WFIRST* observations will be taken in the W146 filter every 15 minutes with an exposure time of 47 s (Penny et al. 2019). *Euclid* has two instruments that can simultaneously observe the same field through a dichroic (Laureijs et al. 2011). The VIS instrument is an optical imager with  $0''.1$  pixels and a wide-bandpass filter roughly covering the  $r$ ,  $i$ , and  $z$  bands (Cropper et al. 2018); the NISP instrument is a near-infrared imager with  $0''.3$  pixels and wide  $Y$ ,  $J$ , and  $H$  filters (Maciaszek et al. 2016). We consider two observing modes for *Euclid*: shallow, high-cadence observations, and deep, low-cadence observations. For the high-cadence observations we assume an exposure time of 100 s in both VIS and NISP- $H$  conducted with a cadence of 30 minutes; with *Euclid*'s expected adjacent field slew times of  $\sim 350$  s (Gómez-Alvarez et al. 2018) this cadence allows four fields to be observed, covering most of *WFIRST*'s nominal fields from Penny et al. (2019).<sup>4</sup> For the deep observations we assume that a field would be observed at four dither points each with an exposure time of 250 s in each instrument, requiring a total of just under 30 minutes of observations for each field. We will consider the possibility of these deep observations being taken at a range of cadences, which would represent observations used to fill gaps in *Euclid*'s observing schedule.

The signal-to-noise ratios (S/Ns) of *WFIRST* and *Euclid* observations were calculated assuming a microlensing source star is drawn from a 10 Gyr,  $[\text{Fe}/\text{H}] = 0.0$  MIST isochrone with *WFIRST* magnitudes (Choi et al. 2016; Dotter 2016; Paxton et al. 2011) at a distance of 8 kpc. *Euclid* magnitudes were assumed to be equal to PanSTARRS  $i$  for VIS, and 2MASS  $H$  for NISP- $H$ , with AB and Vega zero-points handled appropriately. Extinction as a function of position was drawn

<sup>4</sup> This would generate  $\sim 2100$  Gbit day<sup>-1</sup> of data before compression, so *Euclid*'s onboard compression algorithms would need to achieve a compression ratio of  $\sim 2.5$  for crowded bulge images in order for the data to fit within *Euclid*'s regular 850 Gbit day<sup>-1</sup> daily downlink budget; for comparison the RICE and HCOMP compression algorithms of `fpack` achieved compression ratios of 3.0 and 2.9, respectively, on a simulated 16 bit VIS image of the bulge from Penny et al. (2013).

from the map of Gonzalez et al. (2012), and converted to other bands using the Cardelli et al. (1989) extinction law with  $R_V = 2.5$  (e.g., Udalski 2003). Crowding was accounted for by adding a smooth background light component with a surface brightness set by the combined brightness of all stars fainter than magnitude  $m_\lambda$  such that there is fewer than one star per photometric aperture brighter than  $m_\lambda$ , with stars drawn from a population synthesis Galactic model (M. Huston & M. Penny 2019, in preparation). Parameters for *Euclid*'s and *WFIRST*'s instruments were taken from Penny et al. (2013, 2019), respectively, and references therein.

To account for variations in stellar density and extinction, signal-to-noise curves were computed for a number of line of sight within the nominal *WFIRST* fields and averaged. To be used in the average, the S/N for each instrument needed to be larger than 3. The combined *Euclid*  $H$  and VIS S/N was computed by addition in quadrature if both channels produced  $S/N > 3$  before averaging. The average S/N curve for *WFIRST* and each of *Euclid*'s instruments and considered observing modes is shown in Figure 1, as well as the ratio of *Euclid*'s to *WFIRST*'s S/Ns. Although there are variations as a function of magnitude, for the majority of *WFIRST*'s main-sequence source stars (W146  $\sim 20$ –24), *Euclid*'s fast cadence mode would reach an S/N that is a factor of  $\sim 60\%$ – $85\%$  brighter than that of *WFIRST* for brighter stars, while the deep observations would be a factor of 1.8–2.3 better than a single *WFIRST* observation. For main-sequence bulge stars, *Euclid*'s VIS instrument can produce better photometry than the NISP instrument due to its finer pixel scale and lower backgrounds. For simplicity we assume the combination of VIS and NISP observations results in a *Euclid* high-cadence precision that is a factor of 1.33 larger (i.e., worse) than *WFIRST*'s, and its deep photometric precision is  $0.5\times$  *WFIRST*'s (i.e., better).

### 4. Results

Our goal is to test the capability of the simultaneous microlensing observations by *Euclid* and *WFIRST* to constrain microlensing parallaxes, relative to the constraints that *WFIRST* alone would provide. Given a range of possible scheduling constraints, we simulate both high-cadence (30 minutes), continuous *Euclid* observations and occasional, deep *Euclid* measurements with three possible cadences, namely 1, 3, and 7 days. We begin by studying an ideal case where the orbital phase separation between the *Euclid* and *WFIRST* is maximal, i.e.,  $\phi \sim \pi$ . We assume a 20th magnitude source with photometric precision of 0.01 mag in *WFIRST* and 0.01 mag in combined *Euclid* VIS and NISP photometry. Figure 2 shows contours of the fractional parallax uncertainty as a function of event impact parameter and event timescale. Contours in the plot show the locations of  $1\sigma$ ,  $3\sigma$ , and  $5\sigma$  parallax measurements, such that events with impact parameters below the contour have significant parallax measurements. The red contours show the significance of the parallax measurement for only *WFIRST* observations, while the black contours show the significance for both *Euclid* and *WFIRST* measurements. At a given timescale, the y-axis contour position is proportional to the fraction of events for which parallax measurements are possible, i.e., if one only considers events with  $u_0 < 1$  then the contour is the fraction of events for which parallax is measurable. The plotted results show that low-cadence *Euclid* observations taken at least as frequently as one observation per day can enable the measurement of microlensing parallax for

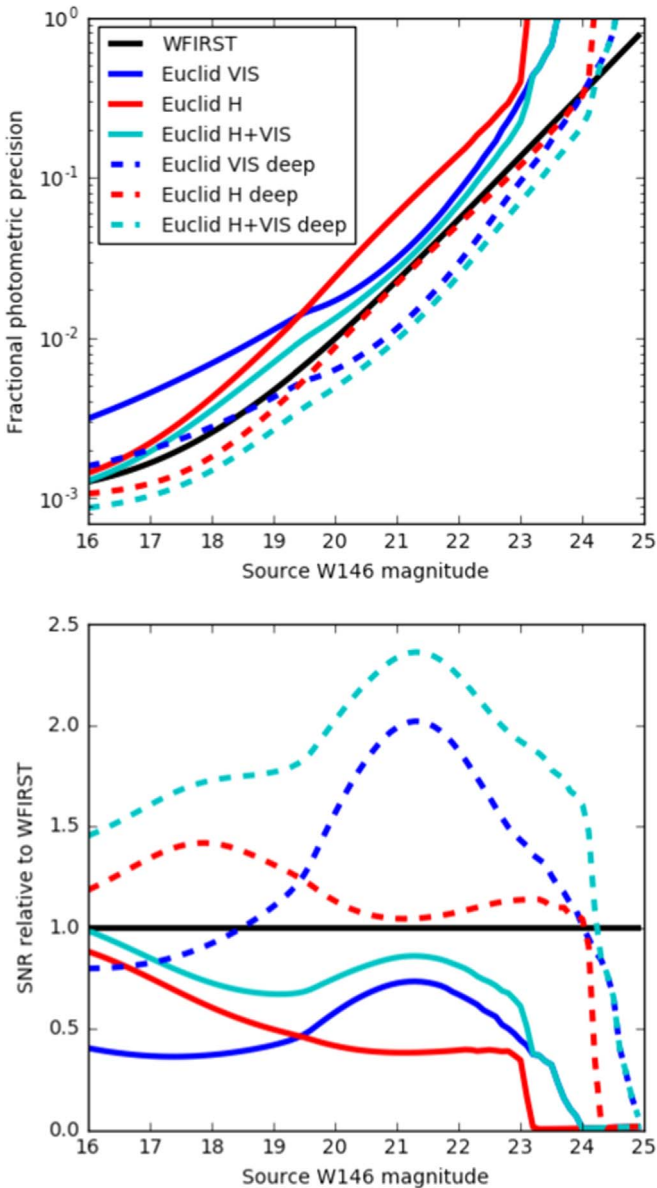


**Figure 1.** Comparison of the photometric precision of *Euclid*'s VIS (blue lines) and NISP-*H* (red lines) observations and their combined precision (cyan lines) to a standard *WFIRST* microlensing observation (black lines). The top panel shows the fractional photometric precision as a function of *WFIRST* W146 source magnitude, accounting for intrinsic source color as determined from a bulge star isochrone, extinction, blending, sky and thermal backgrounds, readout noise, and a systematic noise floor. The bottom panel shows the S/N of *Euclid* observations relative to *WFIRST*. VIS performs better than NISP-*H* for bluer main-sequence stars closer to the sky background, while NISP-*H* performs better for redder giant stars above the background. The combined *Euclid* precision is calculated by combining VIS and NISP measurements in quadrature.

some events with stellar-mass lenses and timescales  $< 4$  days, which is an improvement over *WFIRST* alone. However, only  $\sim 15\%$  of microlensing events are bright enough and only  $\sim 10\%$  have small enough impact parameters for these constraints, and those with the brightest sources are least likely to have direct lens detection masses because the source is more likely to outshine the lens.

Beyond demonstrating detectability, it is valuable to estimate the number of events for which *Euclid* can provide parallax constraints. The top panel of the Figure 3 shows the cumulative

distribution of *WFIRST* source magnitudes for events with planet detections from Penny et al. (2019); the majority have source magnitudes in the range  $W146 \approx 20\text{--}24$ . The bottom panel shows a map of parallax precision plotted as a function of source magnitude and event timescale, assuming several impact parameters and shallow *Euclid* observations with a cadence of 30 minutes or deep observations with a cadence of 1 day. The deep 1 day cadence observations would provide parallax constraints for fewer than the brightest 30% of events with  $u_0 < 0.1$  (i.e., of the order of a few percent of events), and it is unlikely that *Euclid* would have significant holes in its schedule every day, so we do not consider deep, low-cadence observations further.

In contrast, continuous high-cadence observations with *Euclid* are clearly powerful for constraining the microlensing parallax for short-timescale events caused by low-mass lenses. We used the contours in Figure 3 together with joint  $u_0\text{--}W149$  distributions for simulated *WFIRST* free-floating planet detections (S. Johnson et al. 2019, in preparation) to estimate that *Euclid* could measure parallaxes for 17% of *WFIRST*'s free-floating Jupiter-mass planets that it observes ( $t_E \sim 1$  day), and 38% of the 3-Earth-mass planets it observes ( $t_E \sim 0.1$  day). If the occurrence rate of free-floating planets follows the same distribution as bound microlensing planets, i.e., (Cassan et al. 2012),

$$\frac{dN}{dM} = \begin{cases} 0.24(M/95M_{\oplus})^{-0.73} \text{ star}^{-1} & \text{if } M \geq 5M_{\oplus} \\ 2 \text{ star}^{-1} & \text{if } M < 5M_{\oplus} \end{cases}, \quad (8)$$

then *WFIRST* can be expected to detect  $\sim 100$  free-floating planets per decade of mass between 2 Earth masses and 2 Jupiter masses, and  $\sim 50$  total free-floating planets with masses less than  $2M_{\oplus}$ . This number of detections corresponds to an expected detection rate of more than one free-floating planet detection every other day of observations (S. Johnson et al. 2019, in preparation). Of course, the actual occurrence rate of free-floating planets is unknown, but our adopted mass function is roughly commensurate with planetary formation models seen in Veras & Raymond (2012) and Ma et al. (2016). A *Euclid* free-floating planet parallax measurement could therefore be expected once every  $\sim 6$  days of observations. In addition to this, *WFIRST* is also expected to detect  $\sim 3$  bound planets every 24 hr (Penny et al. 2019), so *Euclid* could provide a measurement of a bound or free-floating planet parallax once every 24 hr spent observing microlensing, if we assume a similar parallax detectability for bound planets. If *Euclid* were able to dedicate 20 days of observations to microlensing each time that *WFIRST* was also observing (60 days during its prime mission, and 60 days during an extended mission), it could measure parallaxes for  $\sim 20$  free-floating planets and  $\sim 60$  bound planets.

Finally, we consider the impact of the relative separation of *Euclid* and *WFIRST* in their L2 orbits by varying the orbital phase difference between the two spacecraft that otherwise occupy the same orbit. If the projected separation of the two spacecraft is too small, then *Euclid* would only provide a small increase to the S/N of the annual and L2-orbital parallax, without contributing a much stronger constraint via satellite

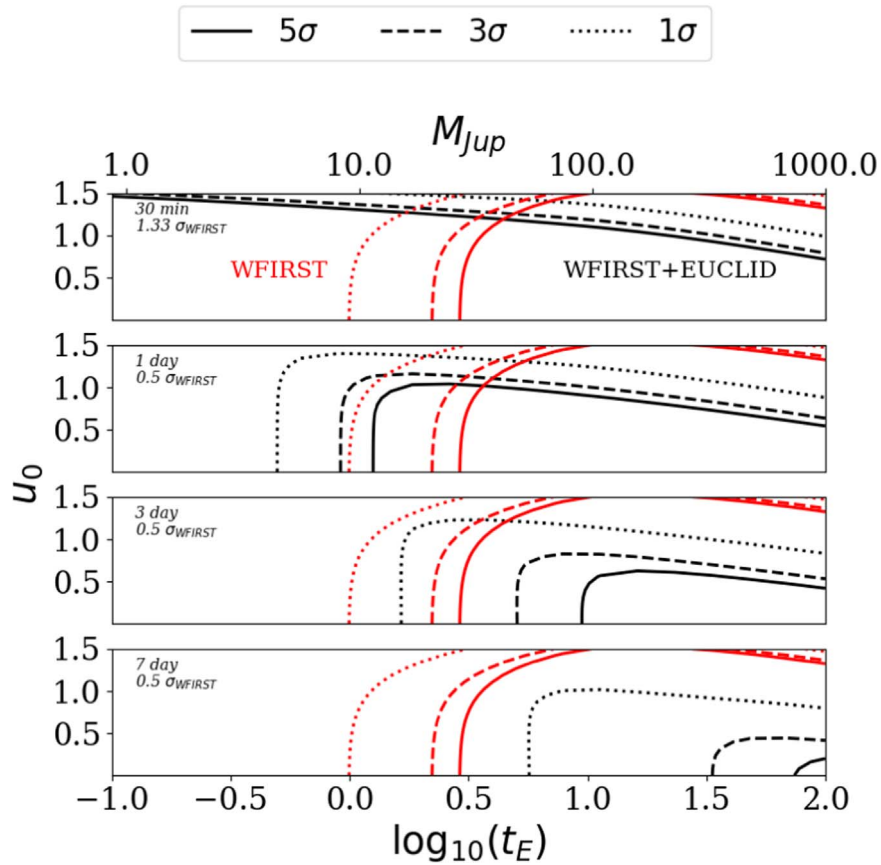


**Figure 2.** Constraints on microlensing parallax provided by simultaneous *Euclid* and *WFIRST* observations as a function of event timescale and impact parameter for several possible *Euclid* observing cadences, for a  $W146 = 20$  mag baseline event (i.e.,  $\sigma_{WFIRST} = 0.01$ ). The short-dashed, long-dashed, and solid lines indicate the maximum impact parameter for which it is possible to make a parallax detection at  $1\sigma$ ,  $3\sigma$  and  $5\sigma$  confidence. The black curves represent *WFIRST* and *Euclid* simultaneous observations, while the red curves represent *WFIRST* observations alone. Note that the *WFIRST* alone plots represent the detection through annual parallax, while the black lines represent the detection through the rotation around L2 only (i.e., annual parallax is ignored). These contours are proportional to the fraction of events for which parallax is measurable. The *EUCLID* cadence and baseline uncertainty are indicated in the top left hand corner of each plot.

parallax. Figure 4 shows the parallax uncertainty as a function of the distance between spacecraft for a microlensing event with  $u_0 = 0.1$ ,  $t_E = 3$  days and a *Euclid* cadence of 1 day. It is clear that even a small distance (e.g.,  $d > 100,000$  km) between the telescopes provides enough constraint for the detection of the microlensing parallax. The required separation shrinks as the lens mass decreases.

## 5. Conclusions

In this Letter we have considered the ability of the *Euclid* spacecraft to provide microlensing parallax measurements by observing contemporaneously with the *WFIRST* microlensing survey. Such measurements will be possible provided the projected separation between *Euclid* and *WFIRST* is larger than 100,000 km. We find that high-cadence observations by *Euclid* for sustained periods of time as short as one day (i.e., longer than the timescale of a free-floating planet event) enable the measurement of parallaxes for large numbers of *WFIRST*'s free-floating planets with short timescales. A significant subset of these would also have finite source measurements of their angular Einstein radii, allowing accurate mass measurements that would be impossible other than for a much smaller number of free-floating planet events that could also be observed from the ground. For each day of simultaneous high-cadence *Euclid* observations we would expect 0.17 free-floating planet parallax measurements. With current launch schedules, *Euclid* and

*WFIRST* could observe simultaneously for a total of 60 days during *Euclid*'s primary mission (less than three percent of the total primary mission), and another 60 days during an extended *Euclid* mission, which would enable parallax measurements for 20 free-floating planets and many more bound planets. For free-floating planets there is no other way to measure their masses.

Due to *Euclid*'s earlier launch date, *WFIRST* is likely to begin observing toward the end of *Euclid*'s main mission, when the likelihood of schedule holes is high (Gómez-Alvarez et al. 2018). Once *Euclid*'s main mission is over, it may be possible to significantly relax *Euclid*'s solar aspect angle constraints, which are designed to maintain the spacecraft's thermal stability. This could significantly increase the length of time *Euclid* could continuously observe microlensing for, and increase the number of free-floating planets for which it can measure parallaxes and masses.

We found that deep, dithered, low-cadence observations by *Euclid*, to be taken in holes in *Euclid*'s regular observing schedule could provide parallaxes for a modest number of microlensing events with timescales. While these observations would go deeper than high-cadence observations in co-added exposures, they would not allow measurement of parallaxes for short-lived and rapidly evolving free-floating planet events. In contrast, while having a higher ratio of overhead to observations, high-cadence observations would be randomly dithered

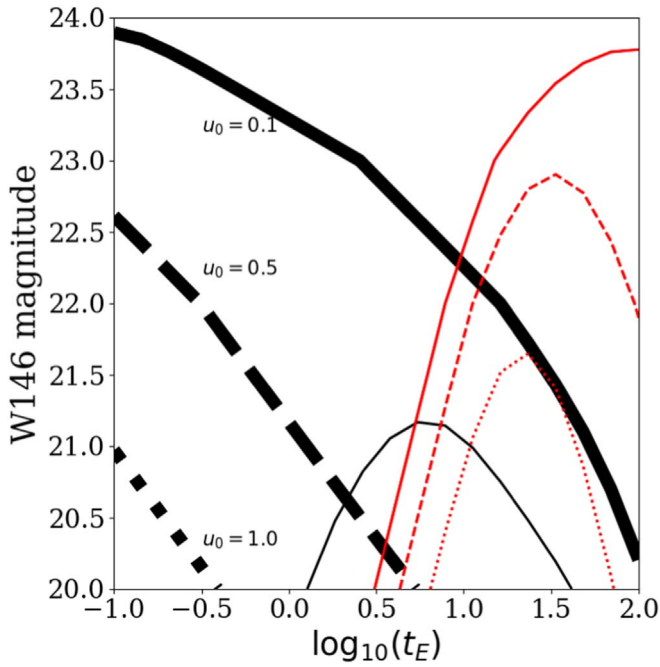


**Figure 3.** Top: cumulative distribution of microlensing source magnitudes from Penny et al. (2019) for events with planet detections. Bottom: microlensing parallax detection limits as a function of the event timescale  $t_E$  and the source magnitude  $W146$ . The black lines represent the  $5\sigma$  detection zones for the *WFIRST* and *Euclid* simultaneous observations. The thick lines represent 30 minute cadences for *Euclid*, and the thin line is 1 day cadence. The plain, long-dashed and small-dashed lines are for  $u_0$  equals to 0.1, 0.5, and 1.0, respectively. The red lines represent the  $5\sigma$  detection zones of *WFIRST* alone through annual parallax.

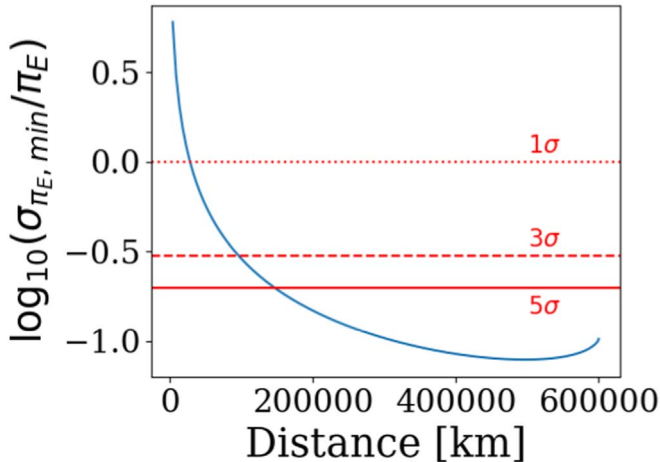


**Figure 4.** Parallax measurement precision as a function of distance between *WFIRST* and *Euclid*. The small-dashed, long-dashed, and plain horizontal lines show  $1\sigma$ ,  $2\sigma$ , and  $3\sigma$  detections. For this simulation,  $u_0 = 0.1$ ,  $t_E = 3$  days, and the baseline photometric precision is  $\sigma_{WFIRST} = 0.01$  mag and  $\sigma_{Euclid} = 0.005$  mag, corresponding to a  $W146 = 20$  mag source. The *Euclid* cadence is set to 1 day.

and could be co-added for depth, while retaining the time-sampling necessary for detecting short-lived free-floating planet events that last only a few hours. We therefore recommend that any microlensing observations taken during gaps in *Euclid*'s schedule be taken in a high-cadence mode, even if the gap is only a few hours long.

We have only considered the ability of *Euclid* to provide free-floating planet parallaxes, but the same principles also

allow the measurement of parallaxes for bound planets at similar rates. Additionally, high-cadence two-filter *Euclid* observations would allow discrimination of potential exoplanet false positives caused by microlensed binary sources (e.g., Gaudi 1998) and for tens of thousands of transiting planets that can be discovered in both *Euclid* and *WFIRST* microlensing observations (McDonald et al. 2014; Montet et al. 2017); in both scenarios false positives have chromatic light curves, while planets have achromatic light curves. Simultaneous *Euclid* observations could also be used to measure the colors of faint Kuiper Belt objects and confirm asteroseismic measurements of bulge giants (Gould et al. 2016). Microlensing surveys also have the potential to detect exomoons (Han 2008; Liebig & Wambsgans 2010). For these objects, complementary observations from *Euclid* to *WFIRST* would be very valuable to break model degeneracies seen in the past (Bennett et al. 2014; Hwang et al. 2018), in addition to the mass measurement. Finally, *Euclid*'s VIS observations would significantly improve *WFIRST*'s host star mass measurements via direct detection of the lens by providing flux measurements in a different bandpass, and measurements of color-dependent centroid shifts (e.g., Bennett et al. 2007; Bhattacharya et al. 2018). Also, the clear distinction between a free-floating planet and a wide binary (i.e.,  $\geq 10$  au) from the analysis of the light curve alone is challenging (Henderson & Shvartzvald 2016; OGLE Collaboration et al. 2019). While it is reasonable to expect the photometry from *WFIRST* and *Euclid* to be precise enough to reveal the subtle asymmetries in the light curves due to wide binaries, a detailed study of the blend flux and the blend proper motion in various bandpasses, in addition to the parallax effects, are a clear benefit of joint *Euclid* observations. Each of these effects is beyond the scope of this letter, but deserve further study.

The authors are grateful for the referee comments that significantly improve the manuscript. Authors thank J.-P. Beaulieu, E. Kerins, J. Rhodes, R. Street, and S. Johnson for fruitful discussions. E.B. gratefully acknowledges support from NASA grants NNX15AC97G and 18-XRP18\_2-0016. M.P. acknowledges the support of NASA grant NNG16PJ32C.

#### ORCID iDs

Etienne Bachelet  <https://orcid.org/0000-0002-6578-5078>  
Matthew Penny  <https://orcid.org/0000-0001-7506-5640>

#### References

- Abell, P. A., Allison, J., Anderson, S. F., et al. 2009, arXiv:0912.0201  
Alcock, C., Akerlof, C. W., Allsman, R. A., et al. 1993, *Natur*, 365, 621  
Aubourg, E., Bairey, P., Bréhin, S., et al. 1993, *Natur*, 365, 623  
Bachelet, E., Bozza, V., Han, C., et al. 2019, *ApJ*, 870, 11  
Bachelet, E., Hinse, T. C., & Street, R. 2018, *AJ*, 155, 191  
Barclay, T., Quintana, E. V., Raymond, S. N., & Penny, M. T. 2017, *ApJ*, 841, 86  
Beaulieu, J. P., Bennett, D. P., Fouqué, P., et al. 2006, *Natur*, 439, 437  
Bennett, D. P., Anderson, J., & Gaudi, B. S. 2007, *ApJ*, 660, 781  
Bennett, D. P., Batista, V., Bond, I. A., et al. 2014, *ApJ*, 785, 155  
Bhattacharya, A., Beaulieu, J. P., Bennett, D. P., et al. 2018, *AJ*, 156, 289  
Bond, I. A., Udalski, A., Jaroszyński, M., et al. 2004, *ApJL*, 606, L155  
Burgess, A. S. M., Moraux, E., Bouvier, J., et al. 2009, *A&A*, 508, 823  
Calchi Novati, S., Gould, A., Udalski, A., et al. 2015, *ApJ*, 804, 20  
Cardelli, J. A., Clayton, G. C., & Mathis, J. S. 1989, *ApJ*, 345, 245  
Cassan, A., Kubas, D., Beaulieu, J. P., et al. 2012, *Natur*, 481, 167  
Choi, J., Dotter, A., Conroy, C., et al. 2016, *ApJ*, 823, 102  
Cropper, M., Pottinger, S., Azzollini, R., et al. 2018, *Proc. SPIE*, 10698, 1069828

- Dotter, A. 2016, *ApJS*, **222**, 8
- Gaudi, B. S. 1998, *ApJ*, **506**, 533
- Gaudi, B. S. 2012, *ARA&A*, **50**, 411
- Gómez-Alvarez, P., Dupac, X., Buenadicha, G., et al. 2018, *Proc. SPIE*, **10707**, 1070712
- Gonzalez, O. A., Rejkuba, M., Zoccali, M., et al. 2012, *A&A*, **543**, A13
- Gould, A. 1994, *ApJL*, **421**, L75
- Gould, A. 2000, *ApJ*, **542**, 785
- Gould, A. 2013, *ApJL*, **763**, L35
- Gould, A., Huber, D., & Stello, D. 2016, *JKAS*, **49**, 9
- Han, C. 2008, *ApJ*, **684**, 684
- Han, C., Jung, Y. K., Shvartzvald, Y., et al. 2018, *ApJ*, **865**, 14
- Henderson, C. B., Poleski, R., Penny, M., et al. 2016, *PASP*, **128**, 124401
- Henderson, C. B., & Shvartzvald, Y. 2016, *AJ*, **152**, 96
- Hwang, K. H., Udalski, A., Bond, I. A., et al. 2018, *AJ*, **155**, 259
- Koshimoto, N., & Bennett, D. 2019, arXiv:1905.05794
- Laureijs, R., Amiaux, J., Arduini, S., et al. 2011, arXiv:1110.3193
- Liebig, C., & Wambsganss, J. 2010, *A&A*, **520**, A68
- Luhman, K. L., Adame, L., D'Alessio, P., et al. 2005, *ApJL*, **635**, L93
- Ma, S., Mao, S., Ida, S., Zhu, W., & Lin, D. N. C. 2016, *MNRAS*, **461**, L107
- Maciaszek, T., Ealet, A., Jahnke, K., et al. 2016, *Proc. SPIE*, **9904**, 99040T
- Marsh, K. A., Plavchan, P., Kirkpatrick, J. D., et al. 2010, *ApJ*, **719**, 550
- McDonald, I., Kerins, E., Penny, M., et al. 2014, *MNRAS*, **445**, 4137
- Mogavero, F., & Beaulieu, J. P. 2016, *A&A*, **585**, A62
- Montet, B. T., Yee, J. C., & Penny, M. T. 2017, *PASP*, **129**, 044401
- Mróz, P., Udalski, A., Skowron, J., et al. 2017, *Natur*, **548**, 183
- OGLE Collaboration, Mróz, P., Udalski, A., et al. 2019, *A&A*, **622**, A201
- Oasa, Y., Tamura, M., & Sugitani, K. 1999, *ApJ*, **526**, 336
- Paczyński, B. 1986, *ApJ*, **304**, 1
- Paxton, B., Bildsten, L., Dotter, A., et al. 2011, *ApJS*, **192**, 3
- Penny, M. T., Gaudi, B. S., Kerins, E., et al. 2019, *ApJS*, **241**, 3
- Penny, M. T., Kerins, E., Rattenbury, N., et al. 2013, *MNRAS*, **434**, 2
- Poindexter, S., Afonso, C., Bennett, D. P., et al. 2005, *ApJ*, **633**, 914
- Refsdal, S. 1966, *MNRAS*, **134**, 315
- Shvartzvald, Y., Udalski, A., Gould, A., et al. 2015, *ApJ*, **814**, 111
- Spergel, D., Gehrels, N., Baltay, C., et al. 2015, arXiv:1503.03757
- Street, R. A., Lund, M. B., Donachie, M., et al. 2018, arXiv:1812.04445
- Sumi, T., Kamiya, K., Bennett, D. P., et al. 2011, *Natur*, **473**, 349
- Udalski, A. 2003, *ApJ*, **590**, 284
- Udalski, A., Szymanski, M., Kaluzny, J., et al. 1993, *AcA*, **43**, 289
- Veras, D., & Raymond, S. N. 2012, *MNRAS*, **421**, L117
- Witt, H. J., & Mao, S. 1994, *ApJ*, **430**, 505
- Wyrzykowski, Ł., Kostrzewa-Rutkowska, Z., Skowron, J., et al. 2016, *MNRAS*, **458**, 3012
- Zapatero Osorio, M. R., Béjar, V. J. S., Martín, E. L., et al. 2000, *Sci*, **290**, 103
- Zhu, W., & Gould, A. 2016, *JKAS*, **49**, 93
- Zhu, W., Udalski, A., Huang, C. X., et al. 2017, *ApJL*, **849**, L31



## Erratum: “WFIRST and EUCLID: Enabling the Microlensing Parallax Measurement from Space” (2019, ApJL, 880, L32)

Etienne Bachelet<sup>1</sup> and Matthew Penny<sup>2</sup>

<sup>1</sup> Las Cumbres Observatory, 6740 Cortona Drive, Suite 102, Goleta, CA 93117, USA; [etibachelet@gmail.com](mailto:etibachelet@gmail.com)

<sup>2</sup> Department of Astronomy, Louisiana State University, Baton Rouge, LA 70803, USA

Received 2020 August 20; published 2020 September 2

The top panel of Figure 3 in the published article was left out of the published version. Here we provide the full Figure 3 showing both panels. The bottom panel is unchanged from that shown in the published article.


The authors thank Radek Poleski and Will Dawson for alerting them to the incorrect figure.

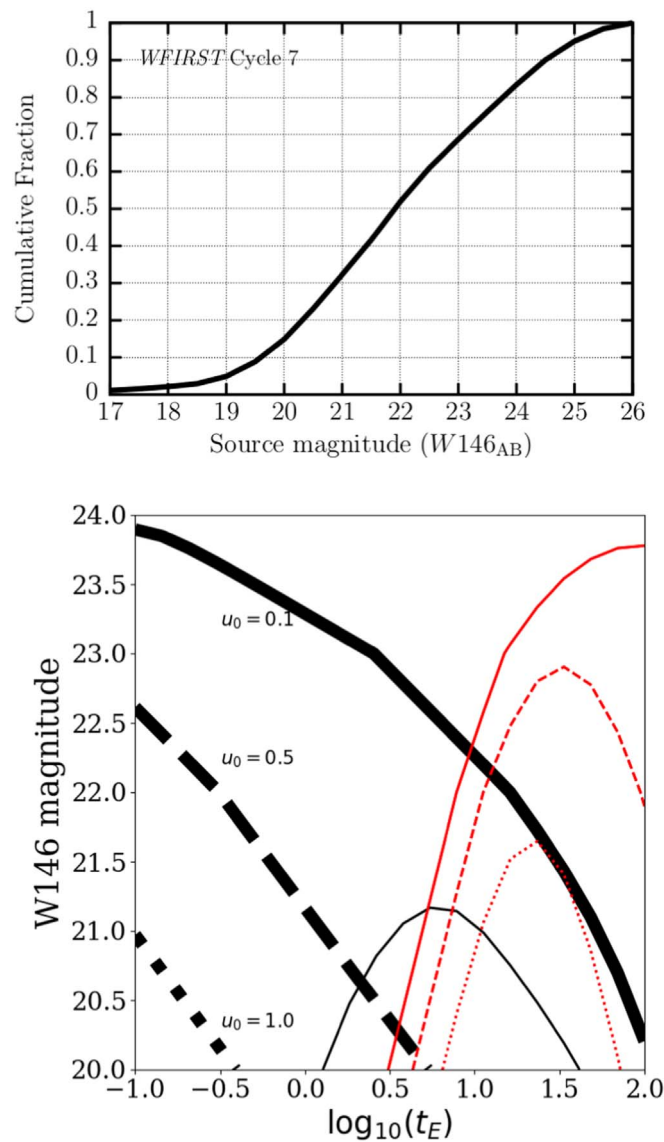


**Figure 3.** Top: cumulative distribution of microlensing source magnitudes from Penny et al. (2019) for events with planet detections. Bottom: microlensing parallax detection limits as a function of the event timescale  $t_E$  and the source magnitude  $W146$ . The black lines represent the  $5\sigma$  detection zones for the WFIRST and Euclid simultaneous observations. The thick lines represent 30 minute cadences for Euclid, the thin line is 1 day cadence. The solid, long-dashed, and short-dashed lines are for  $u_0$  equal to 0.1, 0.5, and 1.0, respectively. The red lines represent the  $5\sigma$  detection zones of WFIRST alone through annual parallax.



### ORCID iDs

Etienne Bachelet  <https://orcid.org/0000-0002-6578-5078>

Matthew Penny  <https://orcid.org/0000-0001-7506-5640>

### Reference

Penny, M. T., Gaudi, B. S., Kerins, E., et al. 2019, *ApJS*, 241, 3